Infinite Cylinder CFD Simulation Verification and Validation

Kevin R. Moore
Brigham Young University

The purpose of this study is to demonstrate proficiency in the areas of verification and validation of CFD in light of an open ended problem definition; Explore laminar flow over a cylinder. I performed this in four steps: First, I developed a simulation according to rules of thumb that validated against experimental data within 2% of the coefficient of drag (*Calculation of Drag Coefficient for Arrays of Emergent Circular Cylinders with Pseudofluid Model* by Cheng). Second, I changed the mesh density to show grid independence. Third, I used the chosen new mesh and changed the domain boundary size to show boundary independence. Fourth, I revisited the temporal and transient solver parameters to verify temporal independence with the changes from the base rule of thumb simulation.

1 Model Overview

With the objective to model laminar flow over a cylinder, I chose a domain that, based on my previous experience, should have been more than capable of accurately resolving the dynamic forces on the cylinder. I chose a bullet shaped domain to save some computational expense and started with an inlet radius of 10 diameters. I chose an exit distance from the cylinder of 30 diameters and a resolved wake distance of 20 diameters. I grossly over-exaggerated the wake distance and did not change it in this study to remove a variable and enable me to focus on improving my proficiency in verification and validation during a reasonable time scale. This is also the case on the prism layer mesh around the cylinder. Figure 1 gives a visual representation of the domain and table 1 gives values for the domain.

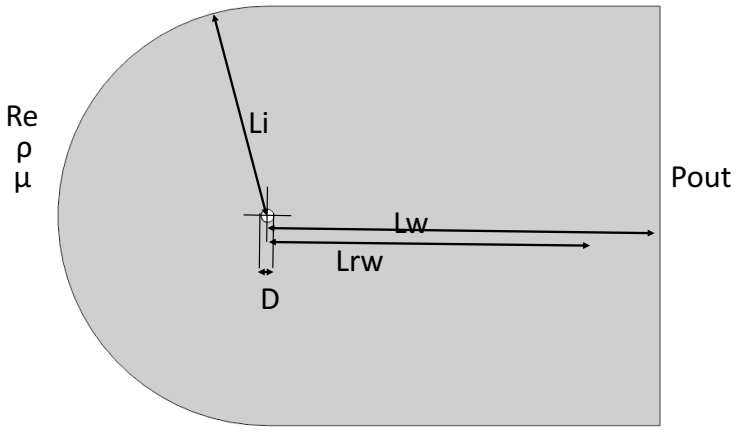

Figure 1: Example mesh grid showing progressive refinement around the flexible beam area.

Name	Value	Description
D	0.01 m	Cylinder Diameter
Li	10-18 D	Inlet Radius
Lw	30 D	Outlet Distance
Lrw	20 D	Resolved Wake Distance
Re	20, 150	Reynolds Number (cylinder diameter)
ρ	1.225 m/kg	Fluid Density
μ	1.855 E-5 Pa-s	Fluid Viscosity

Table 1: Summary of domain geometry and fluid variables.

2 Initial Validated Simulation

Following best practices as described by CD-Adapco, Dr. Ning, and my previous experience, I developed a simulation that validated to within 1.49% for the Re 150 case and 0.27% for the Re 20 case. A plot of the values and the experimental data from Cheng can be seen in figure 2. Due to the nature of the laminar flow, Reynolds number, and mach number, I was able to take advantage of the laminar and incompressible assumptions in the physics conditions. If I had been modeling flow past Re 1E6, significantly more verification would need to be done to include turbulent effects.

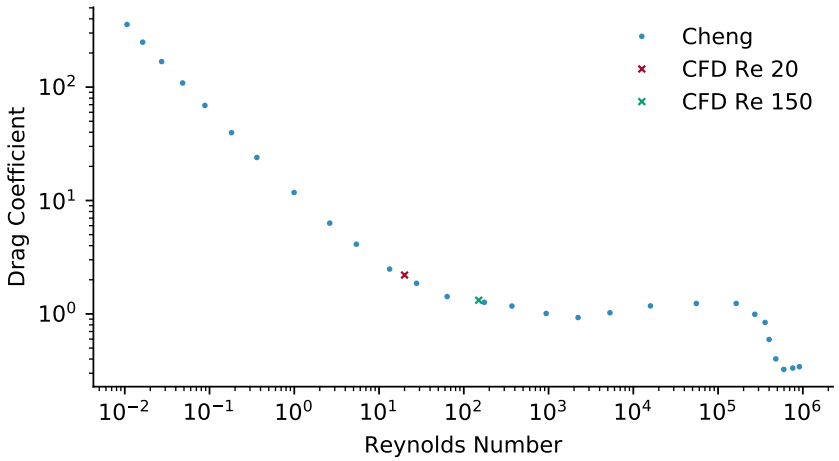

Figure 2: Initial simulation validation against data from Cheng. Validated to within 1.49% for the Re 150 case and 0.27% for the Re 20 case.

I chose an initial inlet radius of 10 diameters, fluid parameters standard for air at sea level, and an inlet velocity to match the required Reynolds number based on the cylinder diameter. I applied the velocity condition to the front continuous surface of the bullet in the x-direction and used a pressure 0.0 pa exit boundary. I chose polyhedral elements with prism meshing, a grid base size of 5 diameters, but refined the mesh around the cylinder to have a target size of 0.1 diameters (2% of the base size). I chose to refine the wake out to 20 diameters with a 10 degree spread and a relative size of 5% of the base size. I found that the default wake refinement was not wide enough in the near-field, so I also added a second wake with a 30 degree spread that extended 3 diameters which gives the meshed domain an arrow like appearance. Blending of the mesh was done with a 20% growth rate to the boundaries, which left boundary cells sometimes smaller than the base size. Figure 3 shows the entire meshed domain.

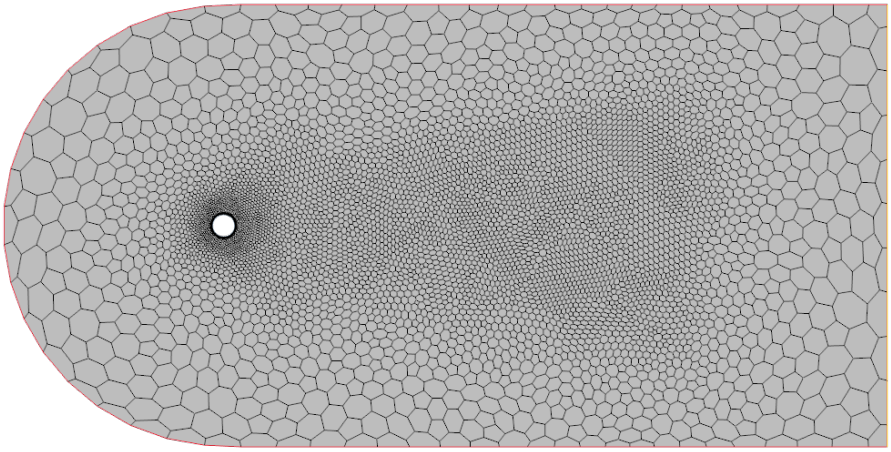

Figure 3: Initial meshed domain shows widened near wake region to accommodate periodic vortex shedding.

I chose 20 prism layers with a 20% growth rate, a minimum thickness of 2.5E-4, or enough to satisfy the y+ condition for both Reynolds numbers and amply resolve the boundary layer. However, while the total thickness of the prism layer was adequate for Re 20, I failed to include enough for Re 150 by a factor of about 2. This doesn't appear to affect the validation solutions though because of the relatively well refined unstructured mesh and prism layer lateral discretization. The boundary layer (besides the lateral discretization based on the target surface size) was not investigated based on the intent and time constraints of the project. The number

of cells for this base case, including the prism layers was 6,163 cells. Figures 4 to 5 show a closer-up image of the cylinder and prism mesh respectively.

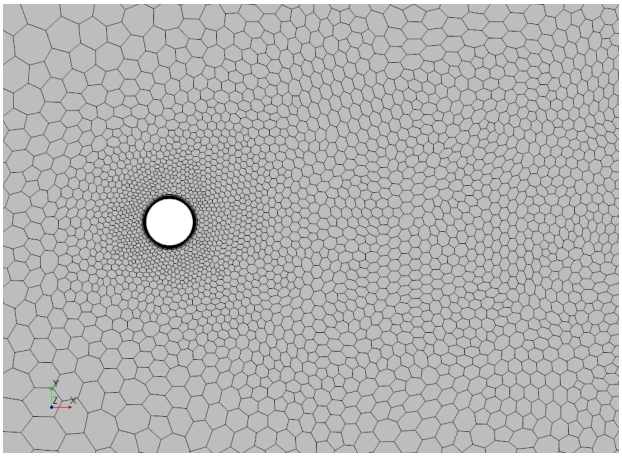

Figure 4: Mesh relatively fine in the regions departing from the cylinder allows for adequate wake refinement.

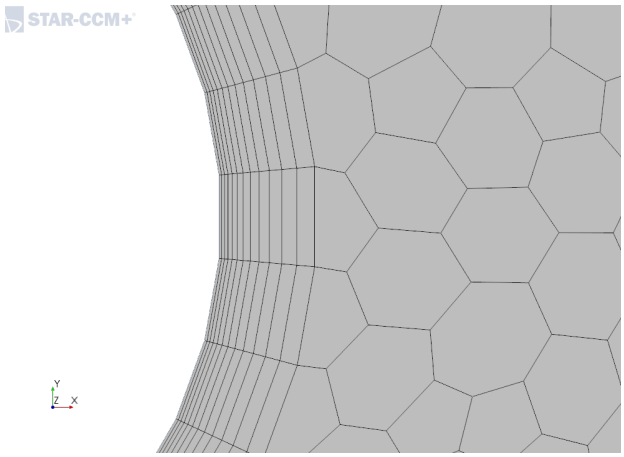

Figure 5: Cell growth from prism layers to unstructured mesh is course though adequate for the baseline mesh.

Because I had the luxury of using a 32 core workstation, I was able to tune the temporal parameters on the fly. I found that the steady state solution as shown by both the force time history as well as the average vorticity in the domain occurred in 5 seconds for Re 150 and 15 seconds for Re 20. These model times correspond to allowing a particle in the wake traverse the entire domain 2.5x for Re 150 and 1.1x for Re 20. Plots of these time histories can be seen in figures 28 to 25 in Appendix A. I changed the inner iterations parameter between 2 and 10 iterations and found 5 to be adequate. I also changed the time step from 0.1 to 0.0005 and found 0.005 to be adequate. With this simulation, I calculated the drag coefficient for both Reynolds numbers and found the agreement to the experimental data to be excellent as discussed above. Figure 6 shows the velocity response and clearly shows the Von-Karman vortex shedding into the wake.

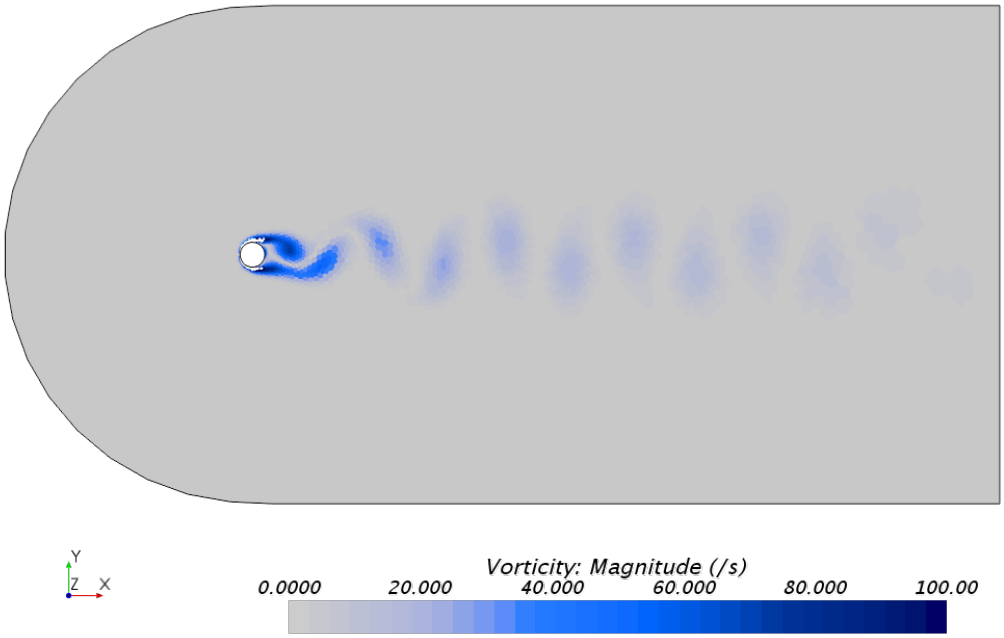

Figure 6: Initial simulation validation against data from Cheng. Validated to within 1.49% for the Re 150 case and 0.27% for the Re 20 case.

In addition to the drag coefficient validation, I calculated the frequency of shedding and compared it to the analytical solution for the flow Reynolds and Strouhal numbers. This version of the simulation gives a frequency of 4.08 Hz while the analytical solution gives 3.9 Hz. With a very good starting point for a simulation that

already accurately models the flow, the following grid, boundary, and temporal convergence studies were simple and straightforward.

3 Grid Independence

Using the baseline simulation, I changed the grid base size to include a range from 10 diameters down to approximately 0.5 diameters, dividing the base size in half at each step. Figures 7 to 8 show the mean drag coefficient with cell number. The simulations appear to be very close to being grid converged with the finest cell count, however the next to last finest mesh with a base size of 0.0125 m, or approximately 45,400 cells performed nearly as well and has significantly less computational cost. For the Re 20 simulation, a much coarser discretization was adequate partly due to the symmetric, steady state, and non-transient nature of the simulation, and partially due to the much lower vorticity. For time considerations in light of the purpose of this study, I chose the next to last discretization as my baseline mesh going forward.

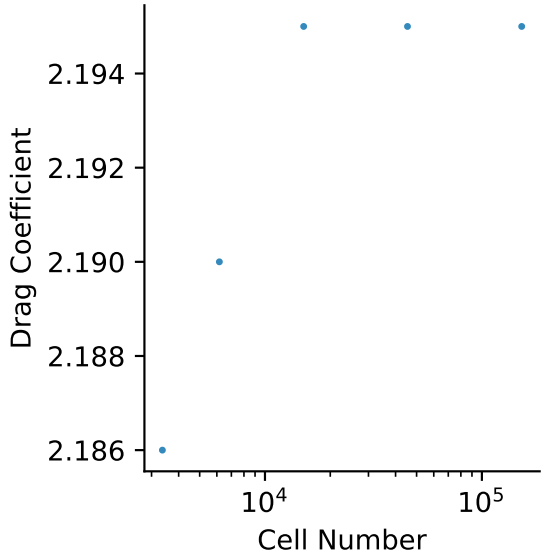

Figure 7: Re 20 case becomes grid independent with just over 10,000 cells.

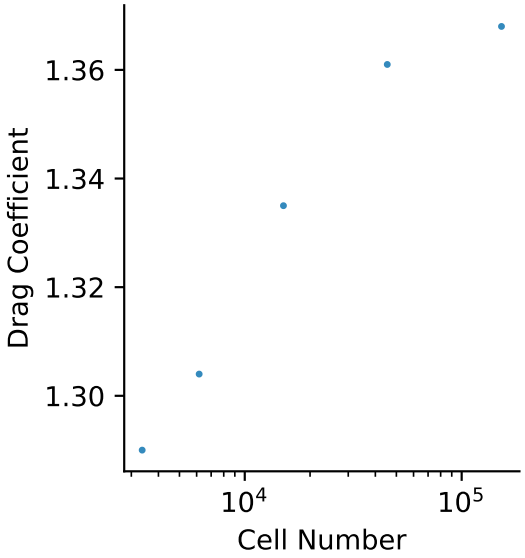

Figure 8: Re 150 case becomes grid independent with slightly more than 300,000 cells

Figures 9 to 10 show the big picture range of mesh discretization. With the discretization I have chosen, the suggested growth rate of 20% between cells is met, while the wake regions are amply refined. This enables an efficient distribution of cells in the regions of high vorticity.

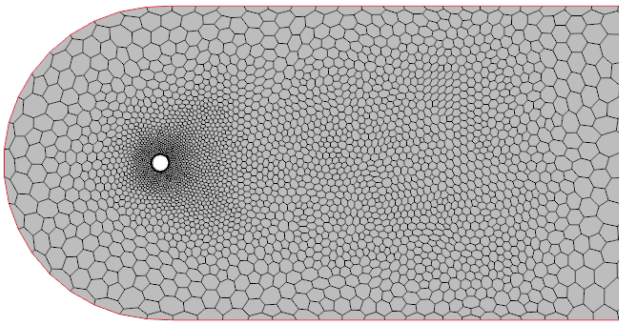

Figure 9: Coarsest mesh consisting of 3,366 cells.

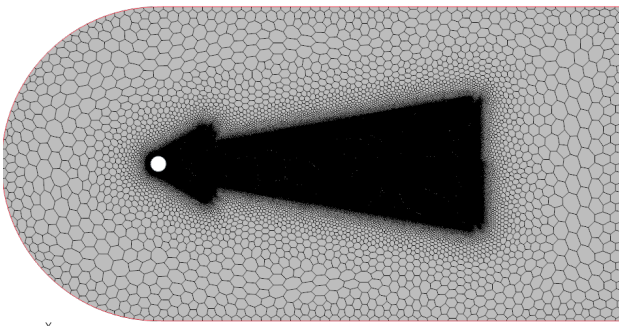

Figure 10: Finest mesh consisting of 153,000 cells.

Figures 11 to 14 give a closer look at the regions around the cylinder and also in the boundary layer mesh for the coarsest and finest meshes. Note the fine lateral discretization in figure 14 which enabled me to get away with not completely including the full boundary layer size in the prism layer mesh for the Re 150 case. Also shown in figure 14, some slight modifications to the prism layer to unstructured mesh transition would need to be made for a more rigorous study, but for the chosen mesh with a base size of twice the finest mesh, the transition was adequate.

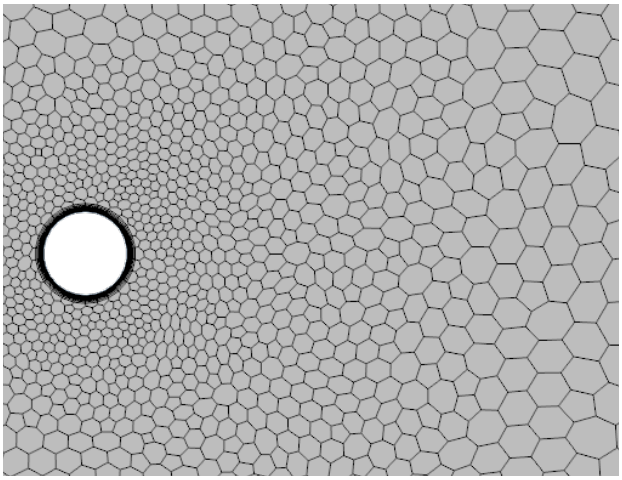

Figure 11: Coarsest mesh includes constant prism layer thickness discretization, but coarse unstructured mesh discretization.

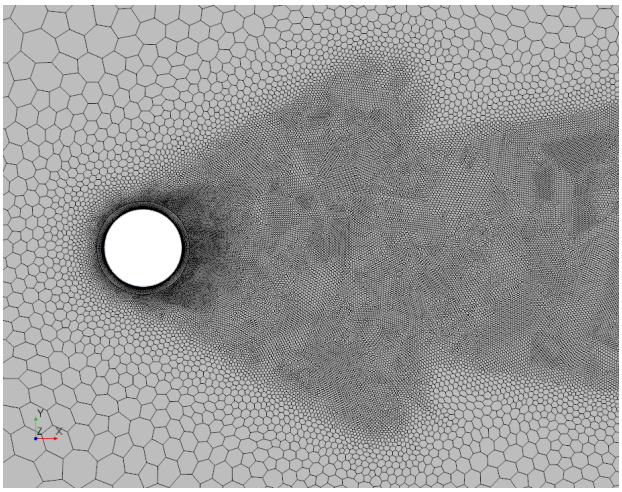

Figure 12: Finest mesh, note the very fine mesh surrounding the cylinder.

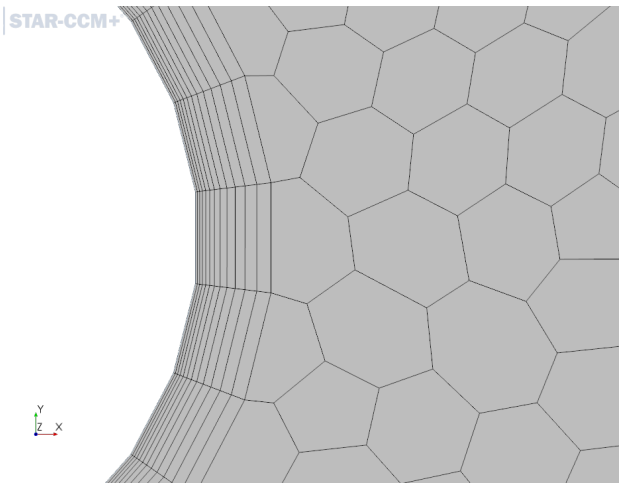

Figure 13: Coarsest prism mesh shows poor transition into unstructured mesh.

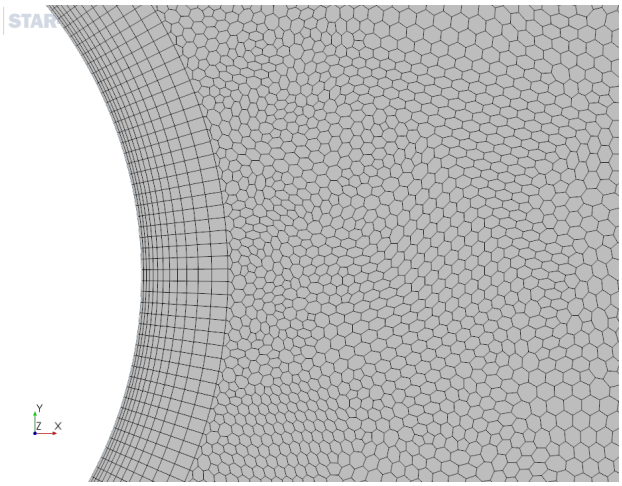

Figure 14: Finest prism mesh shows transition into the unstructured mesh to be slightly too fine.

4 Boundary Independence

While conducting the boundary independence study, it became apparent that my inlet condition of velocity in the x-direction across the entire continuous inlet surface may not have been the best for this study. With the cylinder splitting the flow in the center of the domain, it is likely that a pressure boundary condition on the upper and lower surfaces would have allowed the slight y-direction flow and would have needed a smaller inlet radius. As it is, a very large inlet radius was required with my chosen boundary condition to become boundary independent. After testing up to a radius of 18 diameters, I estimated that a radius of 22 diameters would be necessary, but due to time constraints on the study I chose a radius of 16 diameters. (See figures 15 to 16.) I found this boundary distance to be adequate for force calculations. A to-scale image of the chosen domain of 16 diameters inlet radius is found in figure 1.

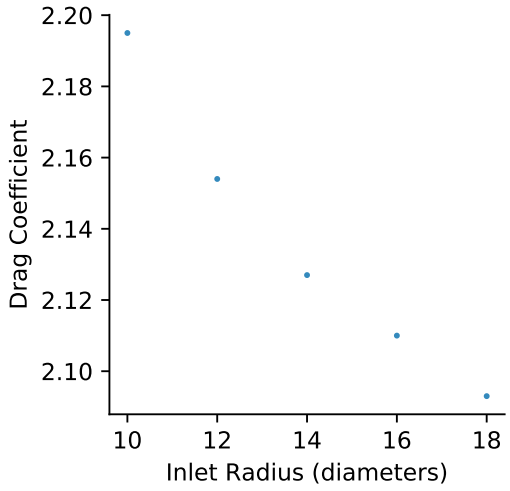

Figure 15: Re 20 case becomes boundary independent with a inlet radius of just over 20 diameters.

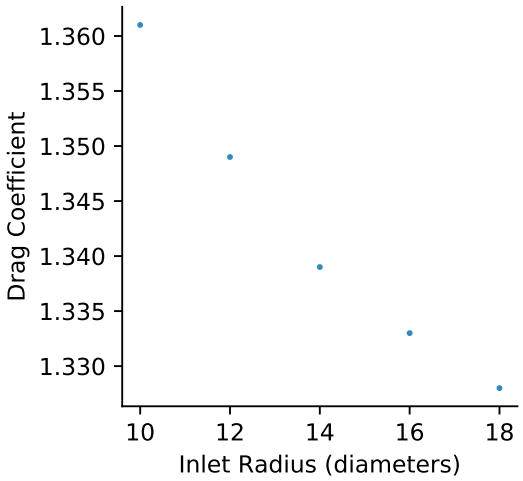

Figure 16: Re 150 case becomes boundary independent with a inlet radius of just over 20 diameters

5 Temporal/Solver Independence

With the mesh and boundary studies finished and a reasonable domain chosen, I more formally revised the temporal and solver criteria for the Re 150 case. Again, for the Re 20 case, the solution has no oscillation, is not affected by temporal parameters, and consequently has not been included it in this section. My time step up until now was 0.005 seconds, so I doubled it, and iteratively halved it until 0.00125 seconds. Second order temporal time As shown in figure 17, a timestep of 0.0025 seconds became temporally independent. On a side note, if I increased the time step above 0.01, I began to see significant numerical damping which removed the vortex shedding altogether.

Figure 18 shows the results of the final condition I changed in this study, the inner iterations. The number of inner iterations is the number of time-frozen steps the solver takes to converge between time steps. I found that 6 was adequate and was unchanged from my original simulation.

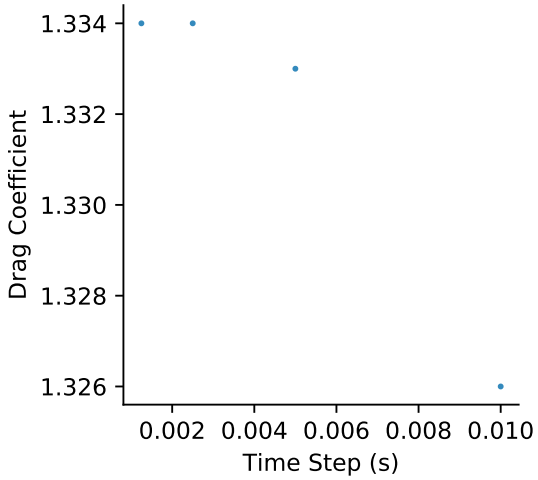

Figure 17: Timestep of 0.0025 was adequate for temporal convergence (Re 150 case).

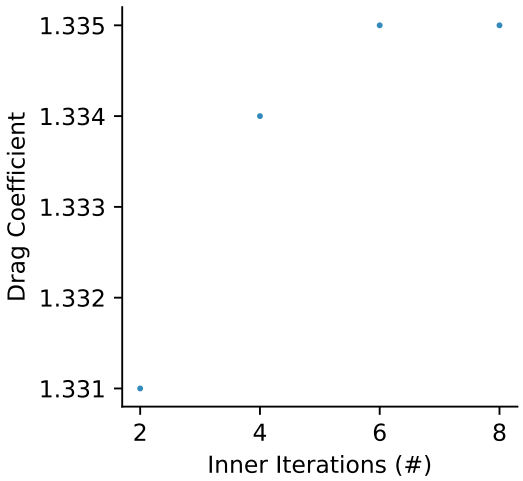

Figure 18: Six inner iterations were adequate for solver convergence (Re 150 case).

6 Conclusions

I was pleased with the outcomes of the study in that: First the results were quite close to real data. Second, the trends for convergence and independency studies followed normal asymptotical trends. Third, the final solution simulation which was deemed adequate by the studies was still simple enough to run in a

reasonable amount of time. Table 2 gives a brief summary of the main parameters used for the final simulation. A skeleton Star-CCM+ .sim and also an html file containing all of the simulation settings can be found at: https://github.com/moore54/ME541.git.

Name	**Value**	**Description**
Base Size	0.0125 m	Mesh base size for which scaling is based upon
Li	16 D	Inlet Radius
Ts	0.0025 s	Temporal discretization
Inner Iterations	5	Number of iterations at each time step
Prism Layers	12	Number of boundary cells designed to resolve boundary layers
Prism Layer Thickness	0.001 m	Total thickness of prism layer cells
Prism Layer Minimum Thickness	2.5E-4 m	Minimum prism cell thickness
Temporal Solver Scheme	Second Order	Method for which temporal discretization is solved
Fluid Type	Constant Density	Solver fluid assumptions
Fluid Flow	Laminar	Solver fluid assumptions
Lw	30 D	Outlet Distance
Lrw	20 D	Resolved Wake Distance
Re	20, 150	Reynolds Number (cylinder diameter)
ρ	1.225 m/kg	Fluid Density
μ	1.855 E-5 Pa-s	Fluid Viscosity

Table 2: Summary of simulation parameters chosen as an adequate case for the given objective. A skeleton Star-CCM+ .sim file for my final simulation and an html file containing all of the simulation settings can be found at: https://github.com/moore54/ME541.git

The ending Von Karman frequency turned out to be 4.18 Hz, slightly larger than the original simulation's 4.08 Hz, and somewhat larger than the analytical 3.9 Hz. I did find though that by decreasing the time step and increasing the number of inner iterations, the frequency was lowered slightly. If my objective in this study was to fully and accurately resolve the wake frequency characteristics, a much more rigorous study would need to be made with experimental Von Karman wake data.

7 Star-CCM+ Tutorials

While I did not complete any tutorials for this assignment I have had previous experience with Star-CCM+ and 2D incompressible flows. The tutorials on moving reference frame and transient fan simulations would be of interest for single propeller validation studies with wake profiles in mind. The tutorials on sound modeling could also be useful if I decide to do CFD while creating a sound model for propeller design optimization.

8 Appendix A: Final Simulation Overview

The following figures show the mesh, velocity and vorticity solutions, and time histories for both the Re 20 and Re 150 cases for the chosen simulation parameters.

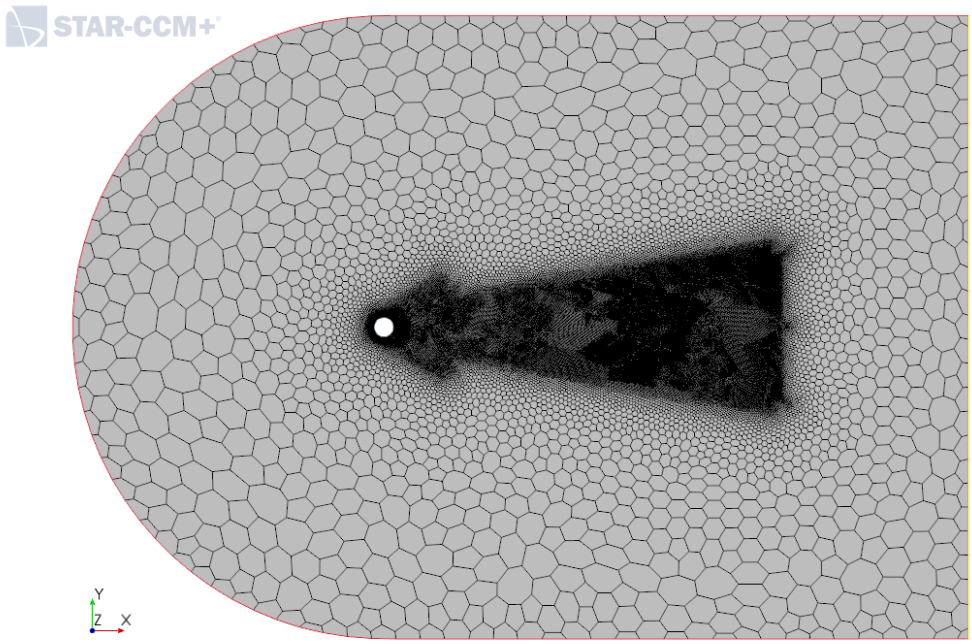

Figure 19: Final simulation full domain mesh.

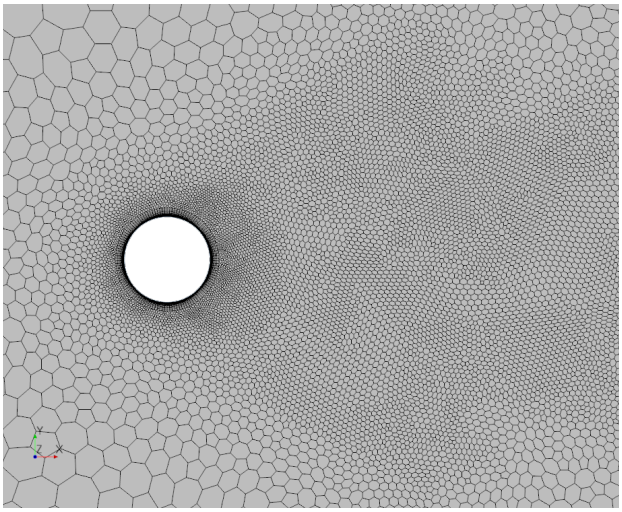

Figure 20: Final simulation near field mesh.

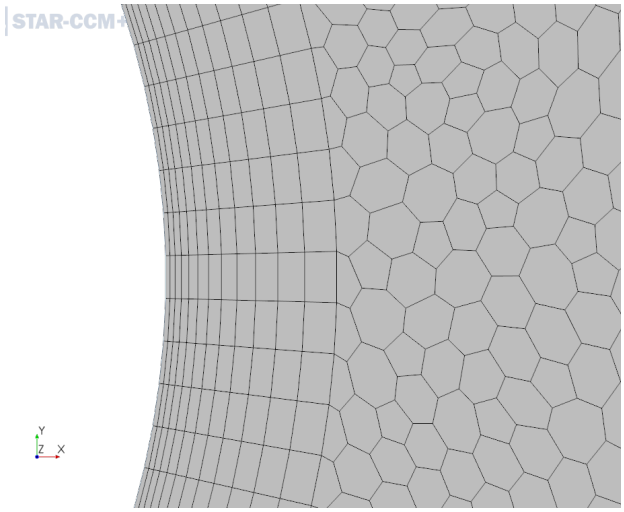

Figure 21: Final simulation boundary layer mesh.

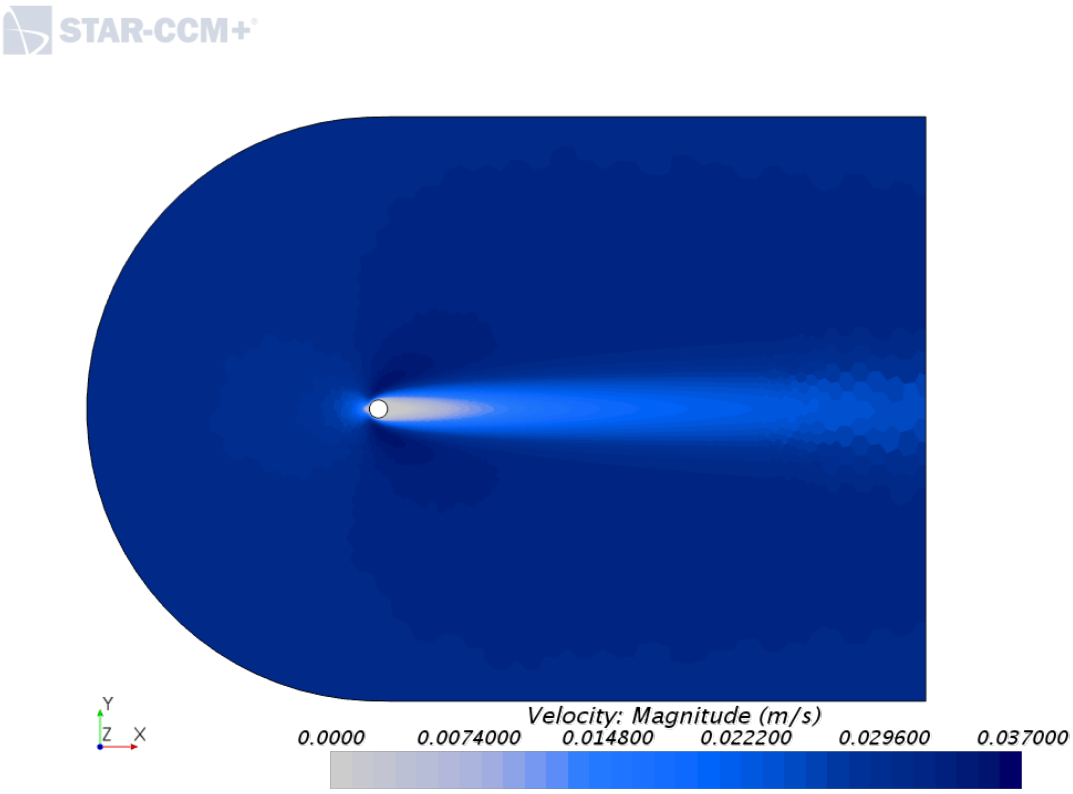

Figure 22: Final simulation velocity field Re 20.

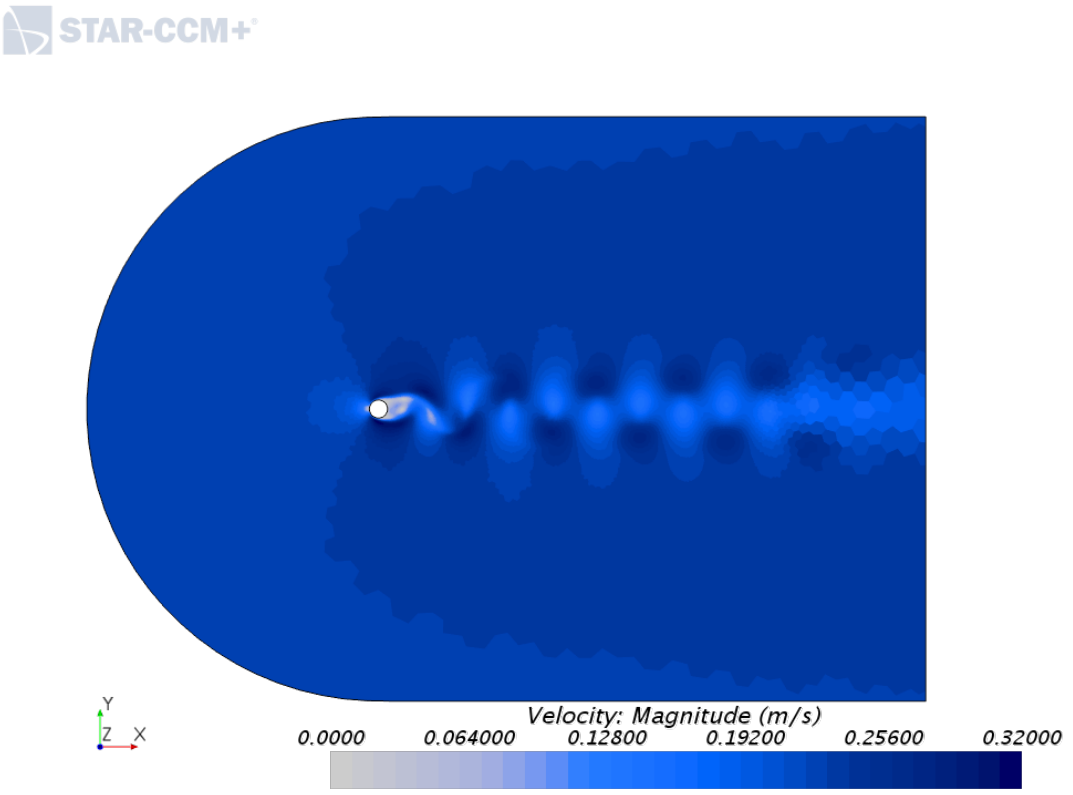

Figure 23: Final simulation velocity field Re 150.

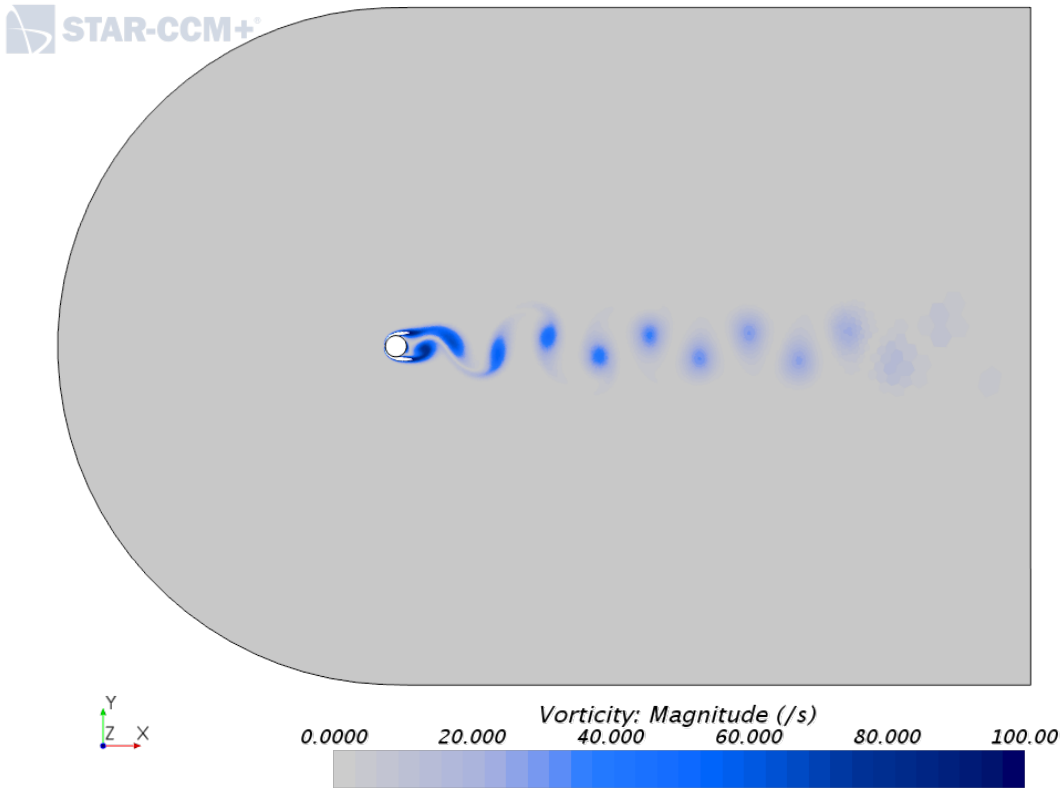

Figure 24: Final simulation vorticity field Re 150.

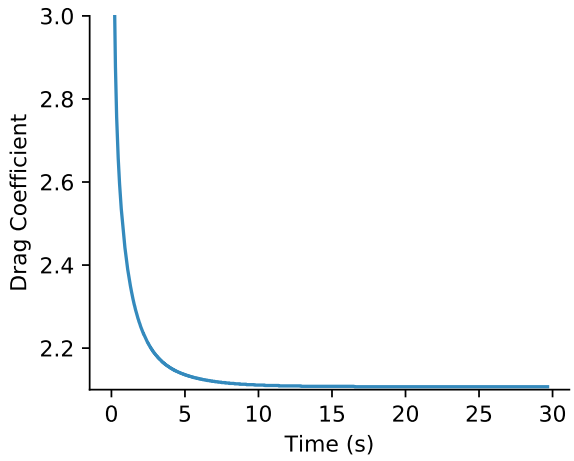

Figure 25: Final simulation drag coefficient as a function of time Re 20.

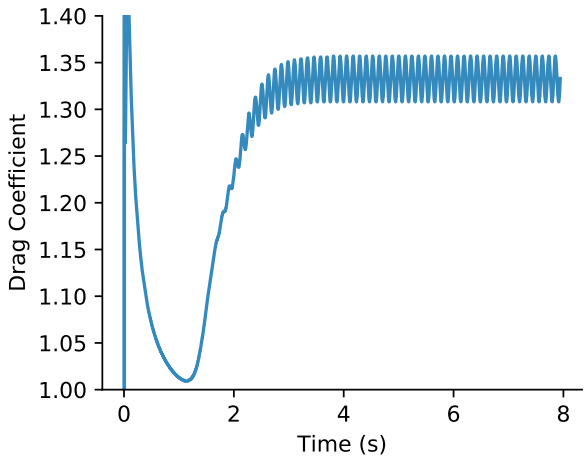

Figure 26: Final simulation drag coefficient as a function of time Re 150.

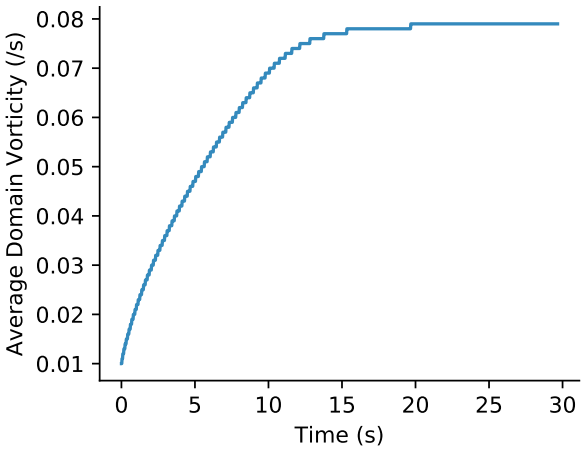

Figure 27: Final simulation average fluid domain vorticity as a function of time Re 20.

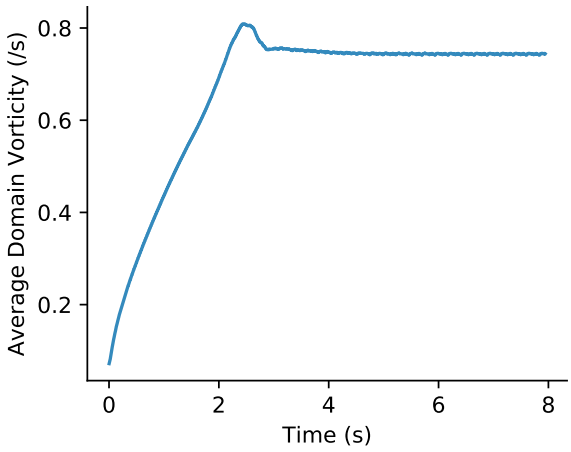

Figure 28: Final simulation average fluid domain vorticity as a function of time Re 150.